PCCP

PAPER

View Article Online
View Journal | View Issue

Cite this: *Phys. Chem. Chem. Phys.*, 2014, **16**, 18570

Why does bromine square palladium off? An *ab initio* study of brominated palladium and its nanomorphology†

Su-Hyun Yoo,[a] Ji-Hwan Lee,[a] Bernard Delley[b] and Aloysius Soon*[a]

Received 31st May 2014,
Accepted 11th July 2014

DOI: 10.1039/c4cp02384f

www.rsc.org/pccp

A first-principles description and prediction of brominated nanocrystals of Pd is presented. In particular, we conducted an extensive study of the adsorption behaviour of Br on various Pd surfaces (including both low and high Miller-index surfaces) as a function of its surface coverage. By coupling our calculated surface energies with *ab initio* (electrochemical) thermodynamics and the Gibbs–Wulff shape model, we find that the relative stability of the Pd surfaces is strongly modified by Br, allowing high Miller-index surfaces of Pd (namely the (210) surface) to become competitively favourable at moderate concentrations of Br. We also show that Pd nanoparticles assume a cube-like crystal shape at high concentrations of Br, exposing mainly the (100) facets with a Br surface coverage of 0.5 ML. This not only confirms and explains recent solution synthesis results, but also provides a quantitative atomic picture of the exposed surface facets, which is crucial in understanding the local surface chemistry of shape-controlled nanoparticles for better nanocatalyst design.

I. Introduction

Transition metals and their alloys have been actively investigated for several decades due to their promising properties, such as surface plasmons and magnetism, and applications toward electrodes and catalysts.[1,2] Because transition metals have multiple oxidation states, they exhibit good catalytic performance towards various chemical reactions, for example, the oxygen reduction reaction (ORR).[3,4] With the advancement of nanoscience and nanotechnology in recent years, nanostructures of transition metals very often give rise to a large enhancement in catalytic performance, due to the fact that the surface-to-volume ratio of these nanomaterials is greatly increased. Given that the overall selectivity of the nanocatalyst can be tuned *via* controlling its exposed surfaces,[5,6] many researchers have now focused not only on gaining an understanding of how to control the size of the nanoparticles, but also on studying its explicit crystal shape or nanomorphology to display various unique chemical and physical properties at the nanoscale.[7–9]

Halides (F, Cl, Br, and I) have been widely used in controlling and manipulating the shape of transition metal nanoparticles. This is due to the fact that halide ions tend to interact strongly with exposed metal facets, explicitly exhibiting a strong influence on its surface energetics and growth kinetics. For instance, it was shown that Cu nanoparticles could assume a nanocube shape under a Cl environment,[10] while another work demonstrated that different halides (Cl and I) could potentially show drastically different polarization effects on Cu surfaces.[11] In addition, the assistance of Au nanorod and nanoplate synthesis by the introduction of Br and I, respectively, have been reported and studied.[12]

Palladium, being one of the (platinum group) late transition metals, has been used in a variety of important technological applications, such as electrodes for multilayer ceramic capacitors,[13,14] hydrogen storage,[15,16] hydrogenation reactions[17] and the Suzuki coupling reaction.[18,19] For pristine nanoparticles of Pd, it has a naturally truncated octahedron shape due to its most stable (111) facets. Recently, it was found that Pd(100) shows a good catalytic performance for a methane oxidation reaction when compared to that of other Pd surfaces, such as the (111), (211) and (321) surfaces.[20] This suggests that a cube-shaped Pd nanoparticle could be a robust catalyst for this type of chemical reaction. Indeed, some recent experiments on the synthesis of cube-shaped Pd nanoparticles have been reported.[12,21,22] In the case of (100)-encapsulated nanocubes of Pd, a KBr solution environment with the precursor Na_2PdCl_4 was found to be essential for achieving these Pd nanocubes.[21–23] The use of the KBr solution as an inorganic capping agent/ligand in these experiments offers a distinct advantage over commonly used organic surfactant bromides (*e.g.* hexadecyltrimethylammonium

[a] *Global E3 Institute and Department of Materials Science and Engineering, Yonsei University, Seoul 120-749, Korea. E-mail: aloysius.soon@yonsei.ac.kr*
[b] *Condensed Matter Theory Group, Paul Scherrer Institut, CH-5232 Villigen, Switzerland*

† Electronic supplementary information (ESI) available. See DOI: 10.1039/c4cp02384f

bromide, CTAB), where the long-chain organic groups could sterically block the local catalytic sites.[24] In addition, cube-shaped Pt–Pd bimetallic nanoparticles have also been realized *via* the use of Br ions.[25]

Although there has been a lot of success in the experimental approaches for the shape-controlled synthesis of these Pd nanoparticles, much of the focus has been on the overall macroscopic description of the synthesis process and neither the local (surface) atomic geometry nor the explicit electronic structure have been given enough attention, which is crucial for chemical catalysis. Notwithstanding, these microscopic details can be studied and probed *via* first-principles electronic structure calculations. Thus, in this present work, we examine the underlying atomic structure and energetics that influence the morphological evolution of Pd nanoparticles under an inorganic Br capping agent environment from first principles.

II. Methodology

A. Computational details

In this work, all density-functional theory (DFT) calculations were performed using the all-electron DMol^3 code[26,27] and the generalized gradient approximation (GGA) to the exchange–correlation functional (PBEsol) reported by Perdew *et al.*,[28] which has been shown to perform well for both bulk and surface properties of transition metals.[29] The Kohn–Sham DFT orbitals were expanded in terms of a double-numerical localized basis set with polarization functions (DNP) where an element-dependent localization cutoff radius was used (*i.e.* 8.55 Bohr for Br and 9.98 Bohr for Pd). Scalar-relativistic corrections have also been included in all calculations.[26,27]

For the surface and adsorption models, we used a symmetric supercell slab approach with a 25 Å vacuum region. The low Miller-index Pd(100), (110), and (111) slabs were composed of 7 atomic layers (AL) with slab depths of 11.7 Å, 8.3 Å, and 13.5 Å, respectively. As for the high Miller-index surfaces, Pd(210) was modelled using 6 atomic layers parallel to the (110) terrace with a slab thickness of 15.7 Å (or an equivalent of 19 AL). Pd(211), Pd(311), and Pd(331) were all modelled using 6 atomic layers parallel to the (111) surface and were thus 13.5 Å (18 AL), 15.3 Å (14 AL), and 12.5 Å (18 AL) thick, respectively. When relaxing the atomic geometries of the low Miller-index Pd surfaces, the 3 inner-most atomic layers of the slab were fixed to their bulk positions while relaxing the other outer-most atomic layers. Likewise for the high Miller-index surfaces, the 7 inner-most atomic layers of Pd(210) and Pd(331) and 6 inner-most atomic layers of Pd(211) and Pd(311) were fixed to their bulk positions. In a similar fashion, the outer-most atomic layers of these high Miller-index surfaces were fully relaxed. To account for the various surface coverages of Br on these Pd surfaces, larger surface supercells of Pd have been employed. We carefully tested the convergence of the required thickness of the low Miller-index surface slab models and extended that to the high Miller-index surface slab models.

The Brillouin-zone integrations were performed using Monkhorst–Pack k-point grids of $(12 \times 12 \times 12)$ for bulk Pd, $(12 \times 12 \times 1)$ for the $p(1 \times 1)$ surface unit cells of Pd(100) and Pd(111), and $(12 \times 8 \times 1)$ for Pd(110). For the $p(1 \times 1)$ surface unit cells of high Miller-index Pd surfaces, we used a k-point grid of $(7 \times 7 \times 1)$ for Pd(210) and Pd(311), $(12 \times 5 \times 1)$ for Pd(211), and $(5 \times 5 \times 1)$ for Pd(331). These k-point grids were then folded accordingly for the larger surface supercells used. We also optimized both the atomic positions and lattice parameters of bulk palladium dibromide ($PdBr_2$) with a k-point grid of $(8 \times 12 \times 1)$. A thermal broadening of 0.03 eV was used to improve the k-point convergence. With this setup, the total energies, forces on atoms and their displacements were converged to within 10^{-6} Ha (2.7×10^{-5} eV), 10^{-4} Ha Bohr^{-1} (5.1×10^{-3} eV Å^{-1}), and 10^{-4} Bohr (5.3×10^{-5} Å), respectively.

B. *Ab initio* (electrochemical) thermodynamics

To study the thermodynamic stability of these Br/Pd surface systems in the immediate Br chemical environment, we employed the well-established *ab initio* atomistic thermodynamics (*ai*AT) method, starting from DFT total energies. This has been discussed in great detail in previous reports,[30–33] thus we will briefly outline this for our system. Firstly, we define the clean surface energy of Pd, γ_{clean}, with

$$\gamma_{clean} = \frac{1}{2A}\left(E_{Pd}^{slab} - N_{Pd}^{slab} E_{Pd}^{bulk}\right), \quad (1)$$

where A is the surface unit area, E_{Pd}^{slab} is the total energy of the clean Pd slab, N_{Pd}^{slab} is the corresponding number of Pd atoms in the slab, and E_{Pd}^{bulk} is the total energy of the bulk Pd.

Next, we calculate the average binding energy of the Br adsorbate on Pd, E_b^{Br}, as well as the change in surface Gibbs free energy of adsorption, ΔG^{ad}, as a function of the change in the chemical potential of bromine, $\Delta\mu_{Br}$, by following these equations:

$$E_b^{Br} = \frac{1}{N_{Br}}\left(E_{Br/Pd} - N_{Pd} E_{Pd}^{slab} - \frac{N_{Br}}{2} E_{Br_2}\right), \quad (2)$$

$$\Delta G^{ad}(\Delta\mu_{Br}) \simeq \frac{1}{2A}\left(N_{Br} E_b^{Br} - \Delta N_{Pd}\mu_{Pd} - N_{Br}\Delta\mu_{Br}\right), \quad (3)$$

where $E_{Br/Pd}$ is the total energy of the Br/Pd system. Here, $\Delta\mu_{Br}$ is the change in the chemical potential of Br with respect to the Br_2 molecule (in the gaseous state), and likewise, E_{Br_2} and N_{Br} are the total energy of the Br_2 molecule and the number of Br atoms in the system, respectively. In passing, the term $\Delta N_{Pd}\mu_{Pd}$ in eqn (3) is only required when the total number of Pd atoms on the specific surface is different from that of the clean surface. We note that the vibrational and configurational effects of these systems have been neglected in this work, whereby the Gibbs free energy has been approximated by the calculated DFT total energy. This approximation has been successfully applied to predict the relative stability of surface structures in other adsorbate–substrate systems[31,34,35] where such effects are deemed to be small and thus will not change the overall conclusion in this work.

Given that these transition metal nanocatalysts often operate under an electrochemical environment (especially in fuel cell applications) as well, it is also interesting to study their nanomorphology evolution under the influence of an electrode potential, U. Within the *ai*AT approach, we use the procedure of Gossenberger *et al.*[36] where the atomic chemical potential, μ, is reformulated with an electrochemical potential, $\tilde{\mu} = \mu + neU$, where e and n are taken as the elementary charge and the charge of the species, respectively. Then, $\tilde{\mu}$ is used to mimic and describe the potential change of the adsorbate in solution with respect to the standard hydrogen potential, ΔU_{SHE}, in standard state (T = 298 K and p = 1 bar). Through this approach, ΔG^{ad} can be expressed using $\Delta U_{\mathrm{SHE}} = U - U_{\mathrm{SHE}}$ instead of the atomic chemical potential, $\Delta\mu_{\mathrm{Br}}$, by the following equation

$$\Delta G^{\mathrm{ad}}(\Delta U_{\mathrm{SHE}}) = \frac{N_{\mathrm{Br}}}{2A}\left(E_{\mathrm{b}}^{\mathrm{Br}} - \frac{1}{2}E_{\mathrm{Br_2}} - e\left(\Delta U_{\mathrm{SHE}} - U^{0}\right)\right), \quad (4)$$

where U^0 is the reduction potential of Br for the redox pair Br_2/Br^- (1.087 V).[37]

C. DFT-based equilibrium nanocrystal shape prediction

We now describe our approach to model the crystal shapes of the Pd nanoparticles in a Br chemical environment. From eqn (1), we include the effect of Br on the clean surface free energy of Pd, γ_{clean}, by adding the ΔG^{ad} term from eqn (3) (or eqn (4) for an electrochemical environment) in the following manner:

$$\gamma_{\mathrm{Br/Pd}}(\Delta\mu_{\mathrm{Br}}, \Delta U_{\mathrm{SHE}}) = \gamma_{\mathrm{clean}} + \Delta G^{\mathrm{ad}}(\Delta\mu_{\mathrm{Br}}, \Delta U_{\mathrm{SHE}}), \quad (5)$$

where $\gamma_{\mathrm{Br/Pd}}$ is now the surface free energy of the Br/Pd surface system which depends on either the atomic chemical potential $\Delta\mu_{\mathrm{Br}}$ or the electrochemical potential ΔU_{SHE}. Having obtained the Br/Pd surface free energies from our DFT calculations using eqn (5), we can now use these energies as *ab initio* input parameters into the Gibbs–Wulff shape model[38] to study the evolutionary equilibrium crystal shape (ECS) as a function of its adsorbate environment[31,33,39] – in both a Br chemical and electrochemical environment. Briefly, the mathematical equation of Gibbs–Wulff theorem is given by:

$$r(d) = \min_{hkl}[\alpha \cdot \gamma(\mu_i)], \quad (6)$$

where $r(d)$ represents the radius of the crystal in the vector (hkl) direction, d, and α is the constant. $\gamma(\mu_i)$ is the surface energy value as a function of the chemical potential of the component i. This then results in the Gibbs–Wulff polygon – a shape-focused theorem (and not on the size explicitly). Without the need to explicitly model the ''real'' nanoparticle (neither its size nor the number of atoms), one can provide an estimation of the nanoparticle ECS as a function of its immediate chemical environment.

It is well known that the size of the nanoparticle plays a huge role in its unique physical and chemical properties. Nonetheless, this is not the main point of this work (albeit also very important). Here, we want to stress how special additives (*e.g.* Br) could help in controlling the shape of the nanoparticles (rather than considering size-effects) and have explicitly addressed this morphological evolution *via* first-principles based ECS predictions. The ECS of the brominated Pd nanoparticle is predicted by considering the adsorption of Br on all seven low and high Miller-index surfaces of Pd, namely the (100), (110), (111), (210), (211), (311), and (331) surfaces of Pd, at various surface coverages of Br.

III. Results and discussion

A. Bulk Pd, molecular Br_2, and clean Pd surfaces

Before studying the adsorption behaviour of Br on Pd, we first investigated the bulk properties of Pd, as well as some of the molecular properties of Br_2. The PBEsol-DFT calculated lattice constant (neglecting zero-point corrections) of bulk fcc Pd is 3.90 Å and this agrees well with the reported experimental value of 3.88 Å.[40] Our calculated bulk modulus and cohesive energy of Pd are 193 GPa and −4.28 eV, respectively, which are also in fair agreement with the experimental values (181 GPa and −3.91 eV),[40,41] and are in-line with other reported theoretical results (204 GPa and −4.43 eV).[40,42] The calculated Br–Br bond length and binding energy of Br_2 are 2.32 Å and −1.32 eV, respectively, and agree closely with reported experimental values of 2.28 Å and −1.22 eV.[41,43]

For the clean surfaces of Pd, we specifically considered the low Miller-index surfaces, namely the (100), (110), and (111) surfaces of Pd, as well as the following high Miller-index surfaces: (210), (211), (311), and (331) of Pd. These faceted surfaces are known to comprise a certain combination of low Miller-index terraces and steps, and their explicit relationship is shown in Fig. 1a. The primitive surface unit cells of these Pd surfaces are also indicated in Fig. 1b to h. Upon relaxing the atomic geometries of these surfaces, we reported their DFT surface energies (*cf.* eqn (1)) shown in Table 1. Here we can see that the surface energies of the low Miller-index Pd surfaces are lower (*i.e.* more stable) than those of the high Miller-index surfaces, and these observations are in-line with previously reported values for Pd,[32] as well as those found for other fcc transition metals (*e.g.* Cu).[47] This is easily rationalized by considering the number of metal bonds cut when generating these surfaces, and it will cost more energy (*i.e.* cutting more surface bonds) to cleave the bulk metal to form these high Miller-index surfaces than the low Miller-index ones.[48,49]

B. Thermodynamical stability of Br/Pd surface structures

To date, no systematic studies of Br adsorption on Pd surfaces have been reported, either experimentally or theoretically. Nevertheless, to build up such a study of Br adsorption on the Pd surfaces mentioned above, we have calculated the average binding energies of Br on Pd surfaces as a function of their surface coverages, ranging from as low as 0.17 up to 1.00 monolayer (ML) surface coverage, for each unique binding site as illustrated in Fig. 1b to h using eqn (2). To consider the energetic stability of Br on these binding sites as a function of its surface coverage, we have calculated close to 100 different Br/Pd surface structures. Given that it becomes tedious and

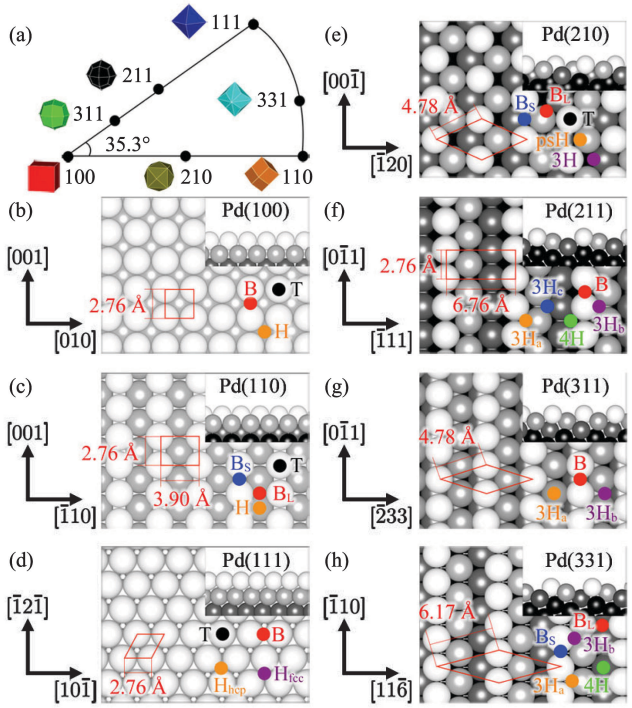

Fig. 1 (a) Stereographic projection of the various high Miller-index surfaces in relation to the low Miller-index surfaces for the fcc lattice. The top- and side-views of the primitive surface unit cells (and the unique adsorbate binding sites) of the (b) (100), (c) (110), (d) (111), (e) (210), (f) (211), (g) (311), and (h) (331) surfaces of Pd are shown. The red lines indicate the primitive surface unit cells with the length of the edges displayed. With regards to the adsorbate binding sites on the low Miller-index surfaces, T represents the top site, B the bridge site, B_S the short bridge site, B_L the long bridge site, H the four-fold hollow site, H_{hcp} the hcp three-fold hollow site, H_{fcc} the fcc three-fold hollow site, and psH the pseudo hollow site. In addition to these sites, for the high Miller-index surfaces, 3H would then represent the three-fold hollow site, 4H the four-fold hollow site, and the subscript letters of H (namely, a, b, and c) represent the first, second, and third kind of sites, respectively.

Table 1 The calculated surface free energies (in eV Å^{-2}), *cf.* eqn (1), of various low and high Miller-index surfaces of clean Pd. The specific nomenclature for the high Miller-index surfaces are also reported[44]

Pd surface	Nomenclature	DFT *xc*-functional	γ_{clean}
(100)	—	PBEsol[a]	0.115
		PBE[b]	0.093
(110)	—	PBEsol[a]	0.122
		PBE[b]	0.097
(111)	—	PBEsol[a]	0.099
		PBE[c]	0.082
		Exp.[c]	0.125
(210)	2(110) × (100)	PBEsol[a]	0.125
(211)	3(111) × (100)	PBEsol[a]	0.115
(311)	2(100) × (111)	PBEsol[a]	0.118
(331)	3(111) × (111)	PBEsol[a]	0.126

[a] This work. [b] Ref. 45. [c] Ref. 46.

cumbersome to report all of the surface structures, we only highlight the average binding energy of the most stable Br/Pd surface structure for each surface as a function of surface coverage in Fig. 2a. By considering the energetics of all of these

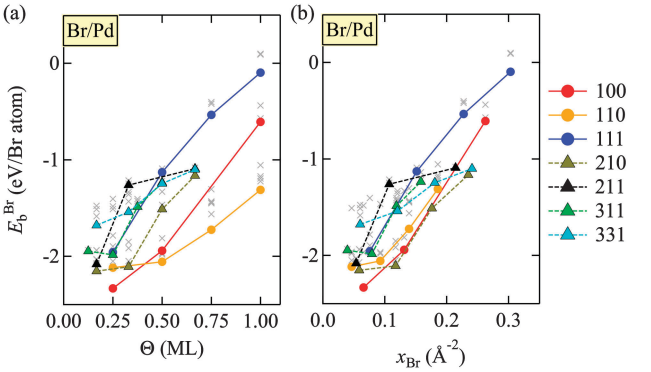

Fig. 2 (a) The average binding energies of Br on Pd surfaces as a function of Br surface coverage, Θ, with respect to half the dissociation energy of Br_2 (*i.e.* $\frac{1}{2}E_{Br_2}$). (b) The same information as in (a) but normalized with respect to the number of Br atoms per area, x_{Br}. The solid lines with filled circles correspond to the adsorption trend of the low Miller-index surfaces: 100 (red), 110 (yellow), and 111 (blue), while the dashed lines with filled triangles correspond to that of the high Miller-index surfaces: 210 (khaki green), 211 (black), 311 (light green), and 331 (cyan). Energetically less-favourable Br/Pd structures are shown as pale gray crosses.

Br/Pd structures, we find that the calculated average binding energy of Br on all of the considered surfaces of Pd increases with the increasing surface coverage of Br. This trend in average binding energies is indicative of a repulsive lateral interaction between surface Br atoms which will be analyzed and described further below in the text.

At low surface coverages of Br, we can see that the average binding energies of the most stable chemisorbed Br on the various Pd surfaces converge to a value near −2 eV, with a small scattered distribution of ±0.5 eV. At 0.25 ML surface coverage, we find that Br binds most strongly at the hollow site (H) on Pd(100) with an average binding energy of −2.33 eV. It is also interesting to find that Br binds strongly at the pseudo-hollow site (psH) on the less stable high Miller-index Pd(210) surface, and is almost as stable as Br on hollow sites for the low Miller-index surfaces of Pd(110) and Pd(111). This is unlike Br on the other high Miller-index surfaces of Pd(311), Pd(331), and Pd(211), where the average binding energies quickly become less favourable as the surface coverage increases above 0.25 ML.

For higher surface coverages of Br, the Br–Br interaction still remains repulsive and increases more rapidly with increasing surface coverages of Br, with Br binding most favourably on the more open Pd(110) surface – more so than on close-packed Pd(111). In particular, for Br/Pd(110), at 0.5 ML, Br occupies the hollow site with an average binding energy of −2.06 eV, and when the surface coverage increases to 0.75 ML, Br then preferentially (but less strongly) binds to mixed hollow and short-bridge sites, with a binding energy of −1.72 eV. Finally, at the full 1 ML, this binding energy value becomes even less favourable (*i.e.* −1.22 eV) when Br adsorbs on the long-bridge sites.

In addition, to discuss the average binding energy trend as a function of the normalized surface area for all of the considered Pd surfaces, we have also plotted this information in Fig. 2b. Here we find that the tendency in the average binding energy

trend (per atom per area) supports our discussion above, and indeed confirms the lateral Br–Br repulsive behaviour with increasing surface coverage of Br.

Having obtained these DFT-calculated average binding energies of Br on Pd surfaces, we now couple these values to the *ai*AT model as described above. Specifically, the change in the Gibbs free energy of Br adsorption for each Pd surface, ΔG^{ad} (*cf.* eqn (3)) is calculated and expressed as a function of the Br chemical potential change, $\Delta\mu_{Br}$, as shown in Fig. 3. In particular, to account for the region of high Br chemical potentials, we consider the formation of bulk palladium dibromide, $PdBr_2$, and calculate its enthalpy of formation to be −0.68 eV per Br atom.

In Fig. 3a, at low $\Delta\mu_{Br}$, the clean Pd(100) surface is the most stable, and with increasing exposure to Br, $p(2 \times 2)$-Br_H (*i.e.* with Br adsorbed at the hollow site at 0.25 ML) is formed when $\Delta\mu_{Br} = -2.33$ eV, followed by the 0.5 ML $p(2 \times 2)$-$2Br_H$ at $\Delta\mu_{Br} = -1.55$ eV, and eventually bulk palladium dibromide ($PdBr_2$) at −0.68 eV. For Pd(110) (in Fig. 3b), upon Br adsorption, a rather small window of surface stability is seen for the 0.25 ML structure ($p(2 \times 2)$-Br_H), followed consecutively by the 0.5 and 0.75 ML structures (*i.e.* $p(2 \times 2)$-$2Br_H$ and $p(2 \times 2)$-$3Br_H$, respectively), and finally bulk $PdBr_2$. As seen in Fig. 3c, Br on Pd(111) shows only one stable surface structure with Br in the hcp hollow site at 0.25 ML ($p(2 \times 2)$-$Br_{H_{hcp}}$), before the onset of bulk $PdBr_2$. For comparison, we have also included the ΔG^{ad} plot for the high Miller-index Br/Pd(210) surface system in Fig. 3d.

It is noticeable that the surface phase transitions start to occur much earlier for the surface systems with an intrinsically less stable clean surface free energy and stronger average binding energy of Br (*e.g.* for Pd(100) and Pd(210)). Although instructive, these ΔG^{ad} provide phase stability information for individual brominated surface structures with reference to their respective clean surfaces. Thus, to relate and compare the relative stabilities of all of the brominated surfaces of Pd in a more unified way, we now consider the adsorbate-modified surface free energy, $\gamma_{Br/Pd}$ of these Br/Pd surface systems *via* eqn (5), and plot the variation of $\gamma_{Br/Pd}$ as a function of $\Delta\mu_{Br}$ and the corresponding electrode potential, ΔU_{SHE}, shown in Fig. 4. For low values of ΔU_{SHE}, the Br_2 gas phase is thermodynamically more stable than the Br^- ion, while for values of ΔU_{SHE} higher than 1.087 V, the Br^- ion dominates, pushing the equation $\frac{1}{2}Br_2 + e^- \leftrightarrows Br^-$ to the right.

C. Environment-dependent morphology of brominated Pd

Given that ΔG^{ad} is always negative in this case, the adsorbate-modified surface free energies are lowered (hence, more stable) compared to γ_{clean}. Using these free energy curves, we then

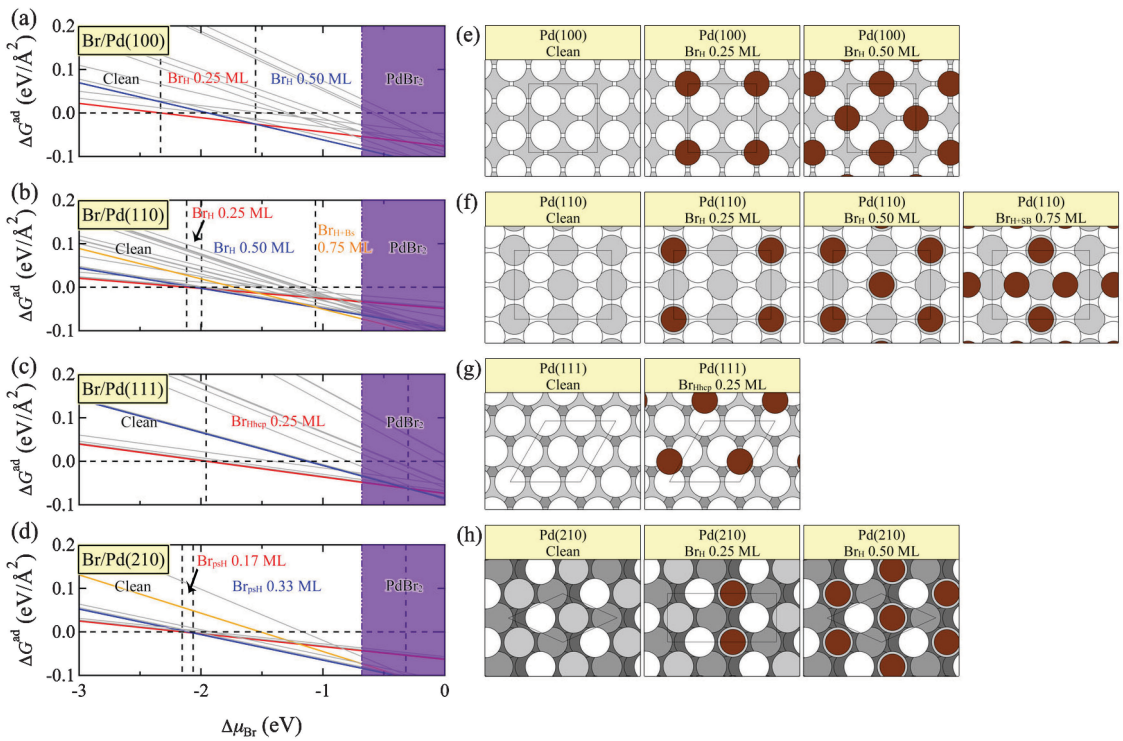

Fig. 3 The calculated Gibbs free energy of the adsorption of Br, ΔG^{ad}, on (a) Pd(100), (b) Pd(110), (c) Pd(111), and (d) Pd(210) as a function of the Br chemical potential change, $\Delta\mu_{Br}$. The horizontal dashed line (at $\Delta G^{ad} = 0$) refers to the stable, clean (Br-free) Pd surface. For each surface, the red, blue and yellow lines indicate the first, second, and third stable surface phase with increasing $\Delta\mu_{Br}$, respectively. Other less stable surface structures are represented as gray lines. To guide the eye, the vertical black dashed lines indicate a surface phase change in stability, while the shaded purple region on the right hand side denotes the region of stability for bulk palladium dibromide, $PdBr_2$. The top-view of the stable surface structures are shown in (e) for Br/Pd(100), (f) for Br/Pd(110), (g) for Br/Pd(111), and (h) for Br/Pd(210). The dark brown circles represent the bromine atoms while the white, light gray, and dark gray circles refer to the first, second, and third outermost Pd surface layers of the slab, respectively.

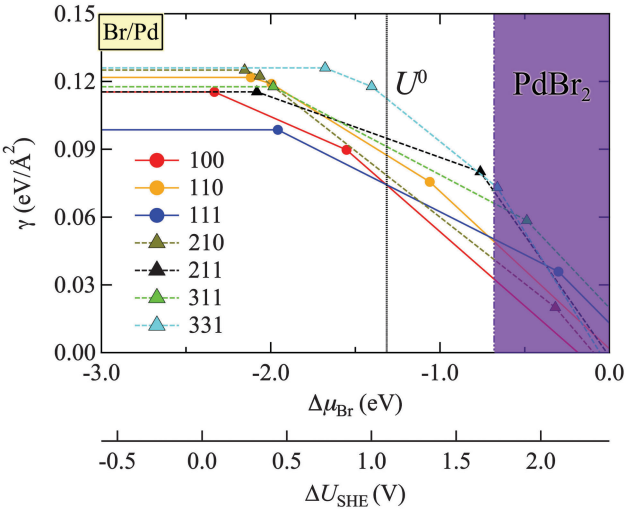

Fig. 4 The calculated surface free energy of brominated Pd surfaces as a function of the Br chemical potential change, $\Delta\mu_{Br}$, and the corresponding electrode potential with respect to the standard hydrogen electrode, ΔU_{SHE}. The variation of surface free energy for the low Miller-index surfaces correspond to the solid lines with filled circles while those for the high Miller-index surfaces correspond to the dashed lines with filled triangles. To guide the eye, the black vertical dashed line indicates the reduction potential of Br (U^0 = 1.09 V), while the shaded purple region on the right hand side denotes the region of stability for bulk palladium dibromide, $PdBr_2$.

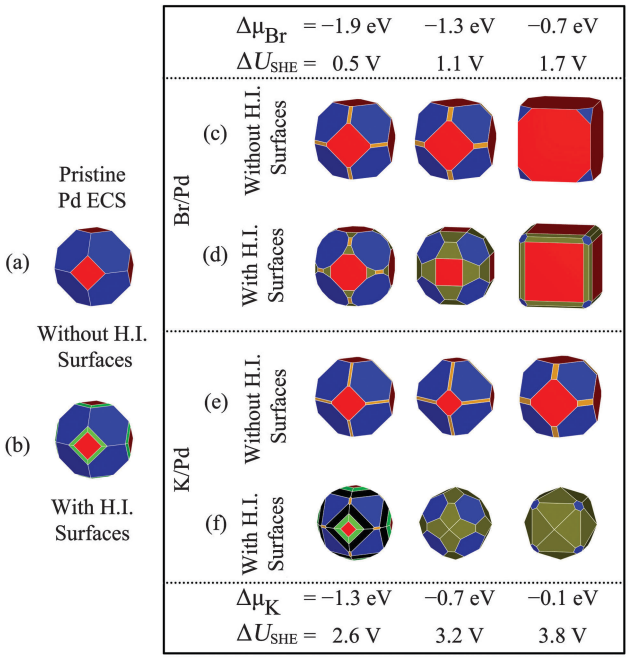

Fig. 5 The predicted morphology evolution of the Pd nanoparticle under the Br (and K) (electro)chemical environment as a function of $\Delta\mu_{Br}$ (and $\Delta\mu_K$) and ΔU_{SHE}. The pristine morphology is described by considering (a) only low Miller-index surfaces, and (b) both low and high Miller-index (H.I.) facets. Changes to the equilibrium crystal shapes are also shown for the two cases: for Br/Pd with the consideration of (c) only low Miller-index surfaces, and (d) both low and high Miller-index surfaces, and likewise in (e) and (f) for K/Pd, accordingly.

predicted and traced the ECS morphological evolution of Br/Pd at the corresponding $\Delta\mu_{Br}$ and ΔU_{SHE}, as shown in Fig. 5. To highlight and emphasize the importance of considering high Miller-index surfaces when modelling the morphology evolution of nanoparticles, we have plotted the ECSs with only low Miller-index surfaces (in Fig. 5a and c), and those with both low and high Miller-index surfaces (in Fig. 5b and d) separately.

Free of Br, the absorbate-free Pd nanoparticle maximizes the exposure of the (111) facet, with the next less stable surfaces (mainly the Pd(100) surface) displayed due to geometric constraints. This is easily rationalized by considering the relative γ_{clean} (in both Table 1 and Fig. 4) where Pd(111) is the most stable clean surface. This results in the so-called (100)-truncated cuboctahedron shape, which is the most common and natural shape for most fcc metallic nanoparticles.[31]

At very low exposures of Br (at $\Delta\mu_{Br}$ = −1.9 eV and ΔU_{SHE} = 0.5 V), this (100)-truncated cuboctahedron is modified slightly by the enlargement of the Br/Pd(100) facet and the small appearance of the Br/Pd(210) surface at the edges. Again, this corroborates our free surface energy curves in Fig. 4 where the (100) surface of Pd is stabilized *via* the adsorption of 0.25 ML of Br at the hollow sites.

At higher $\Delta\mu_{Br}$ (−1.3 eV, and ΔU_{SHE} = 1.1 V), almost equal amounts of the (100), (111) and (210) of Br/Pd are formed, as a result of Br shaping and causing the nanoparticle to become more spherical in shape. This is the result of the large stabilization of both the (100) and (210) surfaces of Pd upon adsorbing Br at 0.25 and 0.33 ML local surface coverage, respectively, as seen in Fig. 4. We strongly stress and contrast the consequence of not considering higher Miller-index surfaces by referring to the different ECSs in Fig. 5c and d where this *rounding* of the nanoparticle would otherwise be overlooked.

At $\Delta\mu_{Br}$ = −0.7 eV (and ΔU_{SHE} = 1.7 V), the nanoparticle ECS completely and drastically transforms into the cubic-like shape, with the (100) surface of Pd encapsulating the whole nanoparticle, Br/Pd(210) lining the edges and very small (111) facets of Pd at the corners of the cube. Once again, the Br/Pd(210) surface structures at the edges would have been omitted if high Miller-index surfaces were excluded in the morphology modeling (*cf.* Fig. 5c and d). This drastic transformation to the nanocube shape is greatly facilitated by the strong Br binding energy modification to the surface free energy of Pd(100), lowering it much more than that of the other surfaces of Pd. This is achieved by adsorbing 0.5 ML of Br at the hollow site of Pd(100). We note in passing that if one were to only consider the average binding energy of Br on Pd as a function of surface coverage (*cf.* Fig. 2) and not include such atomic thermodynamic analysis, one might be easily misled to think that the 0.25 ML structure ($p(2 \times 2)$-Br_H) for Pd(100) should be the most stable (and thus most relevant) structure for further investigation. It is thus important to emphasize that the surfaces/facets used for analysis should be the ones exposed on the nanoparticle (in its appropriate chemical environment).

As reported in ref. 21, KBr solution was introduced in the synthesis of Pd nanocubes, demonstrating that Br anions

served as the key inorganic capping agent for the (100) surface of Pd. Here, we have also investigated the possible role of the K cation which is often ignored. To understand the stability of various K/Pd surface systems, we adsorbed K in the various symmetry-unique sites on the (100), (110), (111), (210), (211), (311), and (331) surfaces of Pd, at various surface coverages of K, as outlined above (*cf.* Fig. 1). We found that the average binding energies of K on Pd are less favorable than those of Br (see the ESI,† Fig. S1), confirming its role as a spectator ion while Br preferentially binds on Pd surfaces. Likewise, we used the concept of *ai*AT with these DFT-derived energetics as inputs and plotted the free energy lines (ESI,† Fig. S3 and S4). For the K/Pd system, the (111) surface of Pd is found to be the most stable surface for all exposures of K, and the resultant ECSs are shown in Fig. 5e (without high Miller-index surfaces of Pd considered) and Fig. 5f (with the inclusion of high Miller-index Pd surfaces). Interestingly, as seen in Fig. 5e, the truncated cuboctahedron nanoshape is preserved when only low Miller-index surfaces are considered, while the importance of the high Miller-index surfaces of Pd is once again demonstrated for higher exposures of K, with the K/Pd(210) facets enveloping the nanoparticle, forming a tetrakishexahedron. In this case, Pd nanocubes are not predicted, and again lends evidence to the spectator role of K ions in the shape-control synthesis of Pd nanocubes, as suggested by previous experiments.[21]

IV. Conclusions

In summary, we studied the chemisorption of Br (and K) on the low and high Miller-index surfaces of Pd, such as (100), (110), (111), (210), (211), (311), and (331), through first-principles DFT calculations. We calculated the surface energies, as a function of the (electro)chemical potential change, accounting for the equilibrium crystal shape evolution of Pd nanoparticles in their immediate chemical environment. We clearly demonstrated the atomic origin of the role of Br in controlling the shape of Pd nanostructures, providing the detailed atomic structure of the Br/Pd(100) exposed facet (*i.e.* $p(2 \times 2)$-$2Br_H$ at 0.5 ML surface coverage), and incontrovertibly showed the important role of high Miller-index surfaces in nanomorphological modeling. Here, we also alluded to the spectator role of the K cation. Given the clear importance and advantages of shape-sculptured nanoarchitectures in many modern-day technologies, having a quantitative atomic picture of the surface chemistry and physics of these nanoparticles will be essential in the rational and systematic design of more selective and active nanocatalysts.

Acknowledgements

The authors gratefully acknowledge the support of the Basic Science Research Program through the National Research Foundation of Korea (NRF) funded by the Ministry of Education, Science and Technology (NRF Grant No. 2014R1A1A1003415). Computational resources have been provided by the Korean Institute of Science and Technology Information (KISTI) supercomputing center through the strategic support program for supercomputing application research (KSC-2013-C3-040). We thank T. Winzer and N. A. Richter for helpful discussions, and J. W. Tan for contributing to the calculations of the K/Pd system.

References

1 A. R. Tao, S. Habas and P. Yang, *Small*, 2008, **4**, 310.
2 S. E. F. Kleijn, S. C. S. Lai, M. T. M. Koper and P. R. Unwin, *Angew. Chem., Int. Ed.*, 2014, **53**, 3558.
3 C. Wang, H. Daimon, T. Onodera, T. Koda and S. Sun, *Angew. Chem., Int. Ed.*, 2008, **47**, 3588.
4 T. H. Yu, T. Hofmann, Y. Sha, B. V. Merinov, D. J. Myers, C. Heske and W. A. Goddard, III, *J. Phys. Chem. C*, 2013, **117**, 26598.
5 K. An and G. A. Somorjai, *ChemCatChem*, 2012, **4**, 1512.
6 M. P. Pileni, *J. Phys.: Condens. Matter*, 2011, **23**, 503102.
7 K. Zhou and Y. Li, *Angew. Chem., Int. Ed.*, 2012, **51**, 602.
8 A. S. Barnard and L. A. Curtiss, *Nano Lett.*, 2005, **5**, 1261.
9 G. A. Somorjai, H. Frei and J. Y. Park, *J. Am. Chem. Soc.*, 2009, **131**, 16589.
10 I. A. Suleiman, M. W. Radny, M. J. Gladys, P. V. Smith, J. C. Mackie, E. M. Kennedy and B. Z. Dlugogorski, *J. Phys. Chem. C*, 2011, **115**, 13412.
11 T. Roman and A. Groß, *Phys. Rev. Lett.*, 2013, **110**, 156804.
12 S. E. Lohse, N. D. Burrows, L. Scarabelli, L. M. Liz-Marzán and C. J. Murphy, *Chem. Mater.*, 2014, **26**, 34.
13 Y. Sakabe, *Curr. Opin. Solid State Mater. Sci.*, 1997, **2**, 584.
14 H. Kishi, Y. Mizuno and H. Chazono, *Jpn. J. Appl. Phys.*, 2003, **42**, 1.
15 S. Kishore, J. A. Nelson, J. H. Adair and P. C. Eklund, *J. Alloys Compd.*, 2005, **389**, 234.
16 M. Yamauchi, R. Ikeda, H. Kitagawa and M. Takata, *J. Phys. Chem. C*, 2008, **112**, 3294.
17 H.-U. Blaser, A. Indolese, A. Schnyder, H. Steiner and M. Studer, *J. Mol. Catal. A: Chem.*, 2001, **173**, 3.
18 Y. Li, X. M. Hong, D. M. Collard and M. A. El-Sayed, *Org. Lett.*, 2000, **2**, 2385.
19 P. Cotugno, M. Casiello, A. Nacci, P. Mastrorilli, M. M. Dell'Anna and A. Monopoli, *J. Organomet. Chem.*, 2014, **752**, 1.
20 A. Trinchero, A. Hellman and H. Grönbeck, *Surf. Sci.*, 2013, **616**, 206.
21 H.-C. Peng, S. Xie, J. Park, X. Xia and Y. Xia, *J. Am. Chem. Soc.*, 2013, **135**, 3780.
22 X. Xia, S. Xie, M. Liu, H.-C. Peng, N. Lu, J. Wang, M. J. Kim and Y. Xia, *Proc. Natl. Acad. Sci. U. S. A.*, 2013, **110**, 6669.
23 Y. Xiong, H. Cai, B. J. Wiley, J. Wang, M. J. Kim and Y. Xia, *J. Am. Chem. Soc.*, 2007, **129**, 3665.
24 W. Niu, L. Zhang and G. Xu, *ACS Nano*, 2010, **4**, 1987.
25 A.-X. Yin, X.-Q. Min, Y.-W. Zhang and C.-H. Yan, *J. Am. Chem. Soc.*, 2011, **133**, 3816.
26 B. Delley, *J. Chem. Phys.*, 1990, **92**, 508.
27 B. Delley, *J. Chem. Phys.*, 2000, **113**, 7756.
28 J. P. Perdew, A. Ruzsinszky, G. I. Csonka, O. A. Vydrov, G. E. Scuseria, L. A. Constantin, X. Zhou and K. Burke, *Phys. Rev. Lett.*, 2008, **100**, 136406.

29 L. Schimka, J. Harl, A. Stroppa, A. Grüneis, M. Marsman, F. Mittendorfer and G. Kresse, *Nat. Mater.*, 2010, **9**, 741.
30 K. Reuter, C. Stampfl and M. Scheffler, *Ab initio* Atomistic Thermodynamics and Statistical Mechanics of Surface Properties and Functions, in Handbook of Materials Modeling, Springer Berlin Heidelberg, 2005, vol. 1.
31 X. Duan, O. Warschkow, A. Soon, B. Delley and C. Stampfl, *Phys. Rev. B: Condens. Matter Mater. Phys.*, 2010, **81**, 075430.
32 F. Mittendorfer, N. Seriani, O. Dubay and G. Kresse, *Phys. Rev. B: Condens. Matter Mater. Phys.*, 2007, **76**, 233413.
33 T. Lee, B. Delley, C. Stampfl and A. Soon, *Nanoscale*, 2012, **4**, 5183.
34 C. Stampfl, *Catal. Today*, 2005, **105**, 17.
35 J. Rogal, K. Reuter and M. Scheffler, *Phys. Rev. B: Condens. Matter Mater. Phys.*, 2007, **75**, 205433.
36 F. Gossenberger, *et al.*, *Surf. Sci.*, 2014, DOI: 10.1016/j.susc.2014.01.021.
37 G. Inzelt, in *Encyclopedia of Electrochemistry, Inorganic Chemistry CH.1. Standard Potentials*, ed A. J. Bard, M. Stratmann, F. Scholz and C. J. Pickett, Wiley-VCH, Weinheim, 2006, vol. 7A.
38 G. Wulff, *Z. Kristallogr.*, 1901, **34**, 449.
39 A. Soon, M. Todorova, B. Delley and C. Stampfl, *Phys. Rev. B: Condens. Matter Mater. Phys.*, 2007, **75**, 125420.
40 L. Schimka, J. Harl and G. Kresse, *J. Chem. Phys.*, 2011, **134**, 024116.
41 C. Kittel, *Introduction to Solid State Physics*, John Wiley & Sons, 8th edn, 2005.
42 A. D. Corso, *J. Phys.: Condens. Matter*, 2013, **25**, 145401.
43 A. Erbil, G. Dresselhaus and M. S. Dresselhaus, *Phys. Rev. B: Condens. Matter Mater. Phys.*, 1982, **25**, 5451.
44 A. Groß, *Theoretical Surface Science: A Microscopic Perspective*, Springer-Verlag Berlin Heidelberg, 2nd edn, 2009, pp. 16–17.
45 N. E. Singh-Miller and N. Marzari, *Phys. Rev. B: Condens. Matter Mater. Phys.*, 2009, **80**, 235407.
46 J. L. F. Da Silva, C. Stampfl and M. Scheffler, *Surf. Sci.*, 2006, **600**, 703.
47 J. L. F. Da Silva, C. Barreteau, K. Schroeder and S. Blügel, *Phys. Rev. B: Condens. Matter Mater. Phys.*, 2006, **73**, 125402.
48 I. Galanakis, G. Bihlmayer, V. Bellini, N. Papanikolaou, R. Zeller, S. Blügel and P. H. Dederichs, *Europhys. Lett.*, 2002, **58**, 751.
49 I. Galanakis, N. Papanikolaou and P. H. Dederichs, *Surf. Sci.*, 2002, **511**, 1.

Electronic Supplementary Material (ESI) for Physical Chemistry Chemical Physics.

Supplementary Information: Why Bromine Squares Palladium Off? An *Ab Initio* Study of Brominated Palladium and its Nanomorphology

Su-Hyun Yoo,[1] Ji-Hwan Lee,[1] Bernard Delley,[2] and Aloysius Soon[1,*]

[1] *Global E3 Institute and Department of Materials Science and Engineering, Yonsei University, Seoul 120-749, Korea*

[2] *Condensed Matter Theory Group, Paul Scherrer Institut, CH-5232 Villigen, Switzerland*

(Dated: June 28, 2014)

I. BULK Pd, MOLECULE Br_2 AND CLEAN Pd SURFACES

TABLE I. Detailed comparison of the lattice constant, cohesive energy, and bulk modulus of bulk Pd (FCC) with experimental and theoretical data.

Bulk Pd	VASP	DMol^3		Ref.			
	PBE[a]	PBE[a]	PBEsol[a]	Exp.	LDA	PBE	PBEsol
Lattice constant (Å)	3.954	3.971	3.903	3.876[b]	3.850[c]	3.950[c]	3.876[b]
(Error % with exp.)	(2.0%)	(2.5%)	(0.7%)	-	-	-	-
Cohesive energy (eV)	-3.702	-3.581	-4.283	-3.907[b]	-5.040[c]	-3.630[c]	-4.426[b]
(Error % with exp.)	(-5.2%)	(-8.3%)	(9.6%)	-	-	-	-
Bulk modulus (GPa)	-	160.92	193.05	181[d]	220 [e]	163 [e]	204[f]
(Error % with exp.)	-	(-2.3%)	(-5.4%)	-	-	-	-

[a] This work
[b] Reference 1
[c] Reference 2
[d] Reference 3
[e] Reference 4
[f] Reference 5

TABLE II. Detailed comparison of the bond length and binding energy of molecule Br_2 with experimental and theoretical data.

Br_2	VASP	DMol^3		Ref.			
	PBE[a]	PBE[a]	PBEsol[a]	Exp.	LDA	PBE	PBEsol
Bond length(Å)	2.307	2.344	2.322	2.283[b]	2.270[c]	-	-
(Error % with exp.)	(1.0%)	(2.7%)	(1.7%)	-	-	-	-
Binding energy (eV)	-1.266	-1.135	-1.318	-1.220[d]	-	-	-
(Error % with exp.)	(-2.3%)	(-7.0%)	(8.0%)	-	-	-	-

[a] This work
[b] Reference 6
[c] Reference 7
[d] Reference 3

TABLE III. Calculated structural parameters for clean surfaces of clean Pd(100), (110), (111), (210), (211), (311), and (331) and the reported reference values.

Pd Surface	Method	Δd_{12} (%)	Δd_{23} (%)
(100)	PBEsol[a]	-1.08	-0.06
	PBE[b]	-1.30	0.00
	Exp.[b]	3.0 ± 1.5	-1.0 ± 1.5
(110)	PBEsol[a]	-8.20	$+2.68$
	PBE[b]	-8.49	$+3.47$
	Exp.[b]	$+5.8 \pm 2.2$	$+1.0 \pm 2.2$
(111)	PBEsol[a]	-0.03	-0.43
	PBE[b]	-0.01	-0.41
	Exp.[b]	$+1.3 \pm 1.3$	-1.3 ± 1.3
(210)	PBEsol[a]	-15.15	-4.04
	PW91[c]	-17	-3
	Exp.[c]	-3	$+7$
(211)	PBEsol[a]	-11.67	-10.52
	PW91[c]	-12.3	-13
(311)	PBEsol[a]	-12.39	$+6.74$
	PW91[d]	-12.4	$+6.9$
(331)	PBEsol[a]	-13.25	-4.22
	PW91[c]	-12	-7.7

[a] This work
[b] Reference 8
[c] Reference 9
[d] Reference 10

II. $E_b(\Theta)$ FOR LOW MILLER-INDEX SURFACES: Br/Pd AND K/Pd

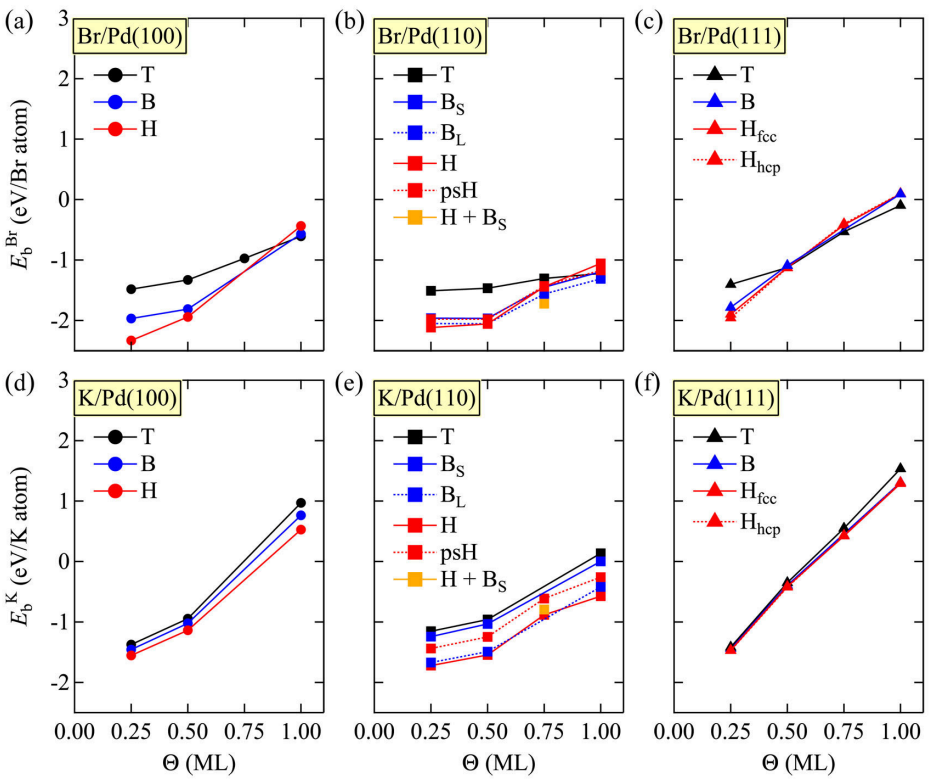

FIG. 1. (Color online) Averaged binding energies of Br (and K) in various symmetry-unique binding sites on Pd surfaces as a function of Br (and K) surface coverage, Θ: (a) Br/Pd(100), (b) Br/Pd(110), (c) Br/Pd(111), (d) K/Pd(100), (e) K/Pd(110), and (f) K/Pd(111).

III. ADSORBATE-SUBSTRATE SYSTEM I: Br/Pd

TABLE IV. Analyzed structural properties for different Br coverage on (100), (110), (111) and (210) Pd surfaces. $d_{\mathrm{Pd-Br}}$ is the average bond length of nearest atoms between Pd and Br. d_{Br1} is the minimum vertical height of Br on utmost Pd surface. Δd_{12} is the interlayer space between the first and second Pd layer. The value is calculated with the center of mass of nth layer. Δd_{23} is the interlayer space between the second and third Pd layer. $E_{\mathrm{b}}^{\mathrm{Br}}$ is the average binding energy of Br.

Br/Pd	Structure	$d_{\mathrm{Pd-Br}}$ (Å)	d_{Br1} (Å)	Δd_{12} (%)	Δd_{23} (%)	$E_{\mathrm{b}}^{\mathrm{Br}}$ (eV/Br atom)
(100)	H (0.25 ML)	2.59	1.66	+0.47	+0.01	−2.33
	H (0.50 ML)	2.63	1.77	+0.22	−0.30	−1.94
(110)	H (0.25 ML)	2.71	1.24	−2.64	+1.15	−2.12
	H (0.50 ML)	2.72	1.30	+1.67	−0.18	−2.06
	H+B_S (0.75 ML)	2.58	1.11	+0.94	−1.13	−1.72
(111)	H_{hcp} (0.25 ML)	2.55	1.97	−0.21	−0.28	−1.96
	H_{hcp} (0.50 ML)	2.69	2.13	+0.03	−0.06	−1.13
(210)	psH (0.17 ML)	2.55	1.44	−8.04	−5.44	−2.15
	psH (0.33 ML)	2.55	1.45	+0.98	−9.10	−2.11
	T+H+B_S (0.50 ML)	2.52	0.63	+1.70	+2.52	−1.51

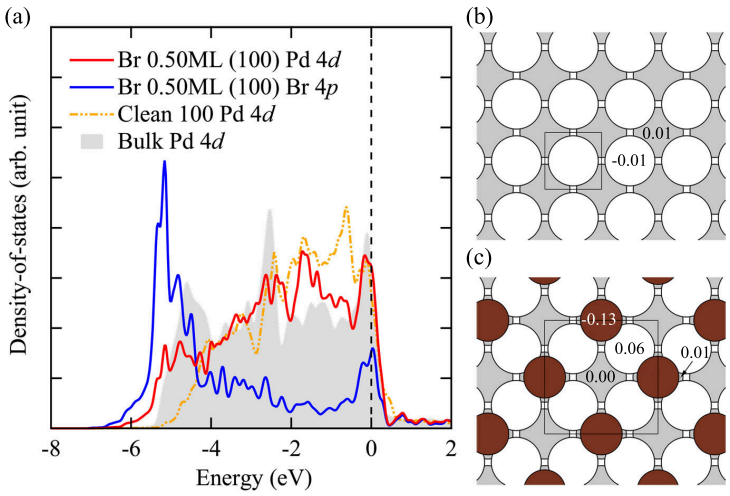

FIG. 2. (Color online) (a) Projected density-of-states (pDOS) for $p(2 \times 2)$-$2\mathrm{Br_H}$, i.e. with Br in the hollow site at the surface coverage of 0.5 ML. The Pd $4d$ pDOS of clean Pd(100) and that of bulk Pd have been included for comparison. Hirshfeld charges (in units of $|e|$) for Pd and Br are shown for (b) clean Pd(100) and (c) $p(2 \times 2)$-$2\mathrm{Br_H}$, where the top-views of the corresponding surfaces are illustrated where the dark brown circles represent the Br atoms while the white and light gray circles are the top-most and second layer Pd atoms, respectively. The more electronegative Br atom is found to gain electrons ($-0.13\,|e|$) from its surrounding Pd atoms ($0.06\,|e|$).

To analyze the nature of bonding, we calculate the projected density-of-states (pDOS) for selected systems and also report the Hirshfeld population charges[11] which have been shown to yield an optimal partitioning of atomic densities which is less sensitive to the quality of the basis set used. In this scheme, integration of the atomic deformation densities (i.e. the total densities of bonded atoms minus that of free atoms) is used to assign the net atomic charges and multipole moments which concisely exemplify the overall charge redistribution.

Since we conclude that $p(2 \times 2)$-$2\mathrm{Br_H}$, i.e. with Br in the hollow site at the surface coverage of 0.5 ML, plays a critical role in the morphology evolution of Pd nanoparticle, we investigate the electronic structure of this structure. To analyze the bonding properties of Br on this surface, we calculate and plot the surface pDOS as well as the surface atomic charges due to the Hirshfeld charges partitioning scheme[11] in Fig. 2. In Fig. 2a, we see that the $4d$ band width of the Pd(100) surface atom is narrowed as compared to that of bulk Pd – commonly understood as a consequence of undercoordination of surface bonds.[12,13] Upon Br adsorption, a renormalization of the Br atomic $4p$ states to lower energies can be seen and a re-brodening of the $4d$ states of the Pd(100) surface atom to lower energies is observed. This hybridization of the Br $4p$ and Pd $4d$ states puts a heavier weight on the

bonding states near the bottom of the Pd $4d$ band while partially filling of the antibonding states near the top of the Pd $4d$ band. This corroborates well with the strong binding of Br on this surface. To understand the charge transfer between Br and Pd on this surface, the Hirshfeld charges for the clean Pd(100) surface and $p(2 \times 2)$-$2\mathrm{Br_H}$ are depicted in Figs. 2b and 2c, respectively. Looking at the corresponding charges, we clearly see that Br, being more electronegative, bears a negative charge ($-0.13\,|e|$) while the nearest surface Pd atoms loose charges ($0.06\,|e|$ each). This charge analysis supports the observations in the pDOS described above.

IV. ADSORBATE-SUBSTRATE SYSTEM II: K/Pd

TABLE V. Analyzed structural properties for different K coverage on (100), (110), (111) and (210) Pd surfaces. $d_{\mathrm{Pd-K}}$ is the average bond length of nearest atoms between Pd and K. d_{K1} is the minimum vertical height of K on utmost Pd surface. Δd_{12} is the interlayer space between the first and second Pd layer. The value is calculated with the center of mass of nth layer. Δd_{23} is the interlayer space between the second and third Pd layer. $E_{\mathrm{b}}^{\mathrm{K}}$ is the average binding energy of K.

K/Pd	Structure	$d_{\mathrm{Pd-K}}$ (Å)	d_{K1} (Å)	Δd_{12} (%)	Δd_{23} (%)	$E_{\mathrm{b}}^{\mathrm{K}}$ (eV/K atom)
(100)	H (0.25 ML)	3.13	2.44	−0.85	+0.21	−1.55
	H (0.50 ML)	3.15	2.47	−0.33	+0.28	−1.14
(110)	H (0.25 ML)	3.18	2.06	−8.20	+3.61	−1.72
	H (0.50 ML)	3.17	2.08	−8.09	+4.30	−1.55
(111)	$\mathrm{H_{hcp}}$ (0.25 ML)	3.05	2.52	+0.52	−0.14	−1.47
(210)	3H (0.17 ML)	3.25	1.75	−20.04	−0.16	−1.63
	3H (0.33 ML)	3.20	1.75	−16.96	−0.77	−1.54

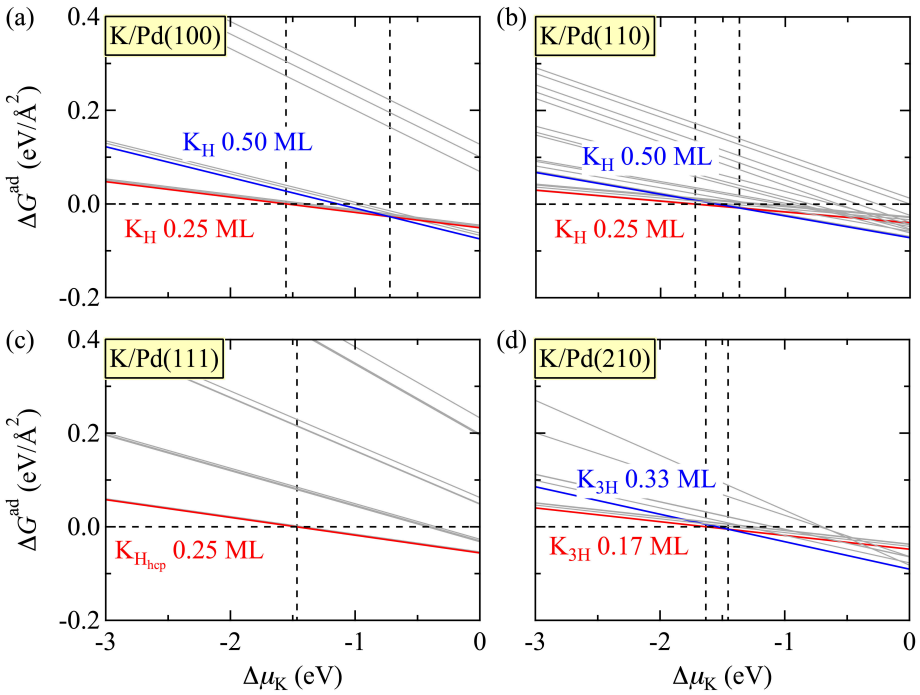

FIG. 3. (Color online) Calculated Gibbs free energy of adsorption of K, ΔG^{ad} on (a) Pd(100), (b) Pd(110), (c) Pd(111), and (d) Pd(210) as a function of the K chemical potential change, $\Delta\mu_{\mathrm{K}}$. The horizontal dashed line (at $\Delta G^{\mathrm{ad}} = 0$) refers to the stable clean (K-free) Pd surface. For each surface, the red and blue lines indicate the first and second stable surface phase with increasing $\Delta\mu_{\mathrm{K}}$, respectively. Other less stable surface structures are represented in gray lines. To guide the eye, the vertical green dashed lines indicate a surface phase change in stability.

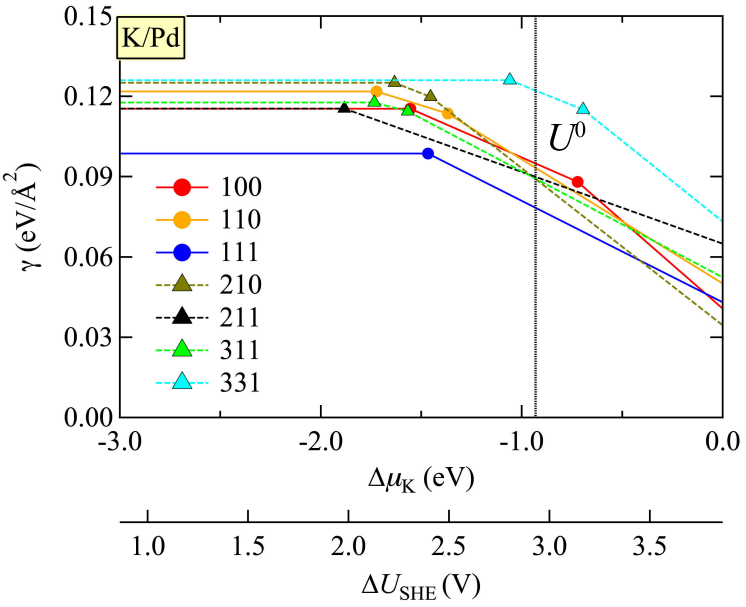

FIG. 4. (Color online) Calculated surface free energy of K/Pd surfaces as a function of the K chemical potential change, $\Delta\mu_{\mathrm{K}}$, and the corresponding electrode potential change, ΔU with respect to the standard hydrogen electrode, U_{SHE}. The variation of surface free energy for the low Miller-index surfaces are traced using solid lines while those for the high Miller-index surfaces are shown in dotted lines. To guide the eye, the black vertical dashed line indicates the oxidation potential of K ($U^0 = 2.924\,\mathrm{V}$).

* Corresponding author. E-mail: aloysius.soon@yonsei.ac.kr

[1] L. Schimka, J. Harl, and G. Kresse, J. Chem. Phys. **134**, 024116 (2011).

[2] J. L. F. D. Silva, C. Stampfl, and M. Scheffler, Surf. Sci. **600**, 703 (2006).

[3] C. Kittel, *Introduction to Solid State Physics* (John Wiley & Sons, Inc, Hoboken. NJ, 2005), 8th ed.

[4] M. Todorova, Ph.D. thesis, Diplom-Physikerin Dissertation, TU Berlin, the Germany (2004).

[5] A. D. Corso, J. Phys.: Condens. Matter **25**, 145401 (2013).

[6] A. Erbil, G. Dresselhaus, and M. S. Dresselhaus, Phys. Rev. B **25**, 5451 (1982).

[7] J.-L. K. Z. S. X. Fan, L. Liu, J. Phys. Chem. C **114**, 14939 (2010).

[8] N. E. Singh-Miller and N. Marzari, Phys. Rev. B **80**, 235407 (2009).

[9] T. S. Rahman, A. Kara, and S. Durukanoğlu, J. Phys.: Condens. Matter **15**, S3197 (2003).

[10] Y. Y. Sun, H. Xu, Y. P. Feng, A. C. H. Huan, and A. T. S. Wee, Surf. Sci. **548**, 309 (2004).

[11] F. L. Hirshfeld, Theoret. Chim. Acta **44**, 129 (1977).

[12] I. Galanakis, N. Papanikolaou, and P. H. Dederichs, Surf. Sci. **511**, 1 (2002).

[13] A. Soon, M. Todorova, B. Delley, and C. Stampfl, Phys. Rev. B **73**, 165424 (2006).